Quasi In-Situ Study of Microstructure in a Laser Powder Bed Fusion Martensitic Stainless Steel

Shahriari, Ayda; Sanjari, Mehdi; Mahmoudiniya, Mahdi; Pirgazi, Hadi; Shalchi Amirkhiz, Babak; Kestens, Leo A.I.; Mohammadi, Mohsen

DOI
10.1007/s11661-024-07353-4

Publication date
2024

Document Version
Final published version

Published in
Metallurgical and Materials Transactions A: Physical Metallurgy and Materials Science

Quasi *In-Situ* Study of Microstructure in a Laser Powder Bed Fusion Martensitic Stainless Steel

AYDA SHAHRIARI, MEHDI SANJARI, MAHDI MAHMOUDINIYA, HADI PIRGAZI, BABAK SHALCHI AMIRKHIZ, LEO A.I. KESTENS, and MOHSEN MOHAMMADI

This study explores the evolution of solidification microstructure of a laser powder bed fusion (L-PBF) martensitic stainless steel during solution annealing and aging. Quasi *in-situ* experiments using electron backscatter diffraction (EBSD) revealed that the finer, more equiaxed microstructure below the melt pool was susceptible to recrystallization and grain growth during solution annealing. The two distinct solidification microstructures below and inside the melt pool converged into a uniform grain morphology after solution annealing and aging processes.

AYDA SHAHRIARI and MOHSEN MOHAMMADI are with the Marine Additive Manufacturing Centre of Excellence (MAMCE), University of New Brunswick, Fredericton, NB, E3B5A3, Canada. Contact e-mail: ashahria@unb.ca MEHDI SANJARI and BABAK SHALCHI AMIRKHIZ are with the Marine Additive Manufacturing Centre of Excellence (MAMCE), University of New Brunswick and also with the CanmetMATERIALS, Natural Resources Canada, 183 Longwood Road South, Hamilton, ON, L8P0A5, Canada. MAHDI MAHMOUDINIYA and HADI PIRGAZI are with the Department of Electromechanical, Systems and Metal Engineering, Ghent University, B9052 Ghent, Belgium. LEO A.I. KESTENS is with the Department of Electromechanical, Systems and Metal Engineering, Ghent University and also with the Department of Materials Science and Engineering, Delft University of Technology, 2628 CD Delft, The Netherlands.
Manuscript submitted September 20, 2023; accepted February 6, 2024.

Published online: 09 March 2024

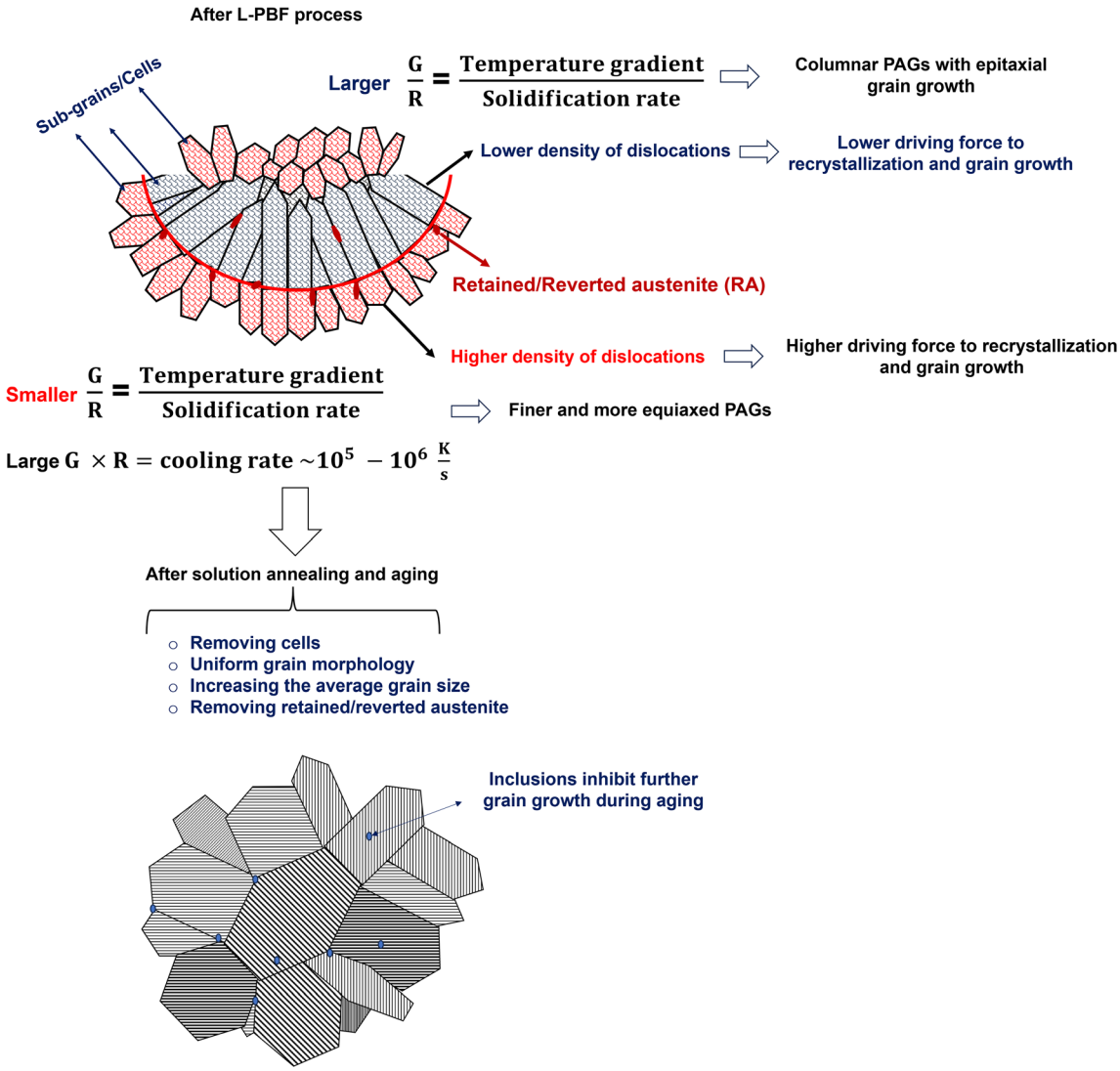

https://doi.org/10.1007/s11661-024-07353-4

CX stainless steel (CX SS) is a low-carbon martensitic stainless steel used in laser powder bed fusion (L-PBF) for additive manufacturing (AM).[1–3] L-PBF with CX SS powder, developed by EOS company, creates a refined microstructure with hierarchical cell structures and small grains.[4–6] During L-PBF, rapid melting and solidification lead to non-equilibrium solidification with a distinct microstructure compared to conventional methods.[7–10] Martensitic structures in low-carbon steels consist of packets, blocks, sub-blocks, and laths.[11–15] Post-heat treatments such as solution annealing and aging are necessary to achieve a homogenized microstructure and improved mechanical properties.[13–22] This study employs quasi *in-situ* electron backscatter diffraction (EBSD) to analyze the crystallographic characteristics of an L-PBFed martensitic Fe–Cr–Ni alloy before and after annealing and aging treatments. It aims to investigate the impact of heat treatments on anisotropic solidification structures, solid-state transformations, recrystallization, and grain growth in L-PBFed steels. By understanding the role of L-PBF solidification in solid-state transformation mechanisms, this research contributes to filling the existing knowledge gap.

A horizontally printed rod-shaped specimen (φ 12 mm × 120 mm) was fabricated using an EOS M290 L-PBF machine and CX stainless steel (CX SS) powder. The powder, spherical and gas atomized, had volume equivalent sphere diameters of d_{10} = 16.33 μm, d_{50} = 26.27 μm, and d_{90} = 42.37 μm. Figure 1 shows

the printed specimens and the CX SS powder composition. The process parameters ensured dense parts with minimal defects (the mean density is 99.68 ± 0.05). A 5 × 5 × 0.5 mm^3 section in the *X-Z* plane (Figure 1) underwent heat treatment, *i.e.*, solution annealing at 900 °C for 1 hour, air quenching, and aging at 550 °C for 3 hours, followed by air quenching. Quasi *in-situ* EBSD observations were conducted on a region marked with microhardness indents before and after heat treatments (Figure 1). The sample underwent heat treatment in an electric furnace with an argon atmosphere to prevent oxidation. After each heat treatment, slight polishing with 0.05 μm colloidal silica suspension was performed for repeated EBSD measurements in a specific region, removing less than 1 μm from the surface.

EBSD scans were performed using an FEG-SEM with a TSL OIM 8 system. EBSD scans, covering a 425 × 425 μm^2 area, were recorded with a 200 nm step size. A smaller 100 × 100 μm^2 area within was scanned with a 50 nm step size (Figure 1). A comprehensive analysis involving EBSD measurements was conducted on an area, yielding a total of 5,215,977 points. The average confidence index (CI) for the entire analyzed region was calculated to be 0.94. Notably, CI serves as a reliability measure for orientation determination, assigned to each data point. A Grain CI Standardization method was applied as a clean-up procedure for all EBSD measurements. It is essential to emphasize that this clean-up method does not alter the crystallographic orientation but enhances the confidence index. Moreover, a cropped melt pool was isolated from the overall analyzed area. In this specific region, comprising 727,489 points, the OIM 8.1.0 system was utilized. The clean-up process was applied similarly, yielding an average CI of 0.91, with 171,156 points in area A and 139,527 points in area B. Grain definition in EBSD involved setting a 5 deg grain tolerance angle and a Minimum Grain Size of 2 points for each grain group. The method combined misorientation and minimal points. Grain size diameter was calculated assuming grains as circles. The average grain diameter was computed by summing the equivalent diameters of each grain and dividing it by the total number of grains.

The sample reference system is also shown in Figure 1. To recreate parent austenite grains (PAGs), a unique methodology and code originally developed by Gomes *et al.*[23] was employed. This approach is designed specifically for the reconstruction of PAGs from their martensitic microstructures. Transmission electron microscopy (TEM) was used to observe martensitic laths with 200 nm thin electron-transparent samples obtained *via* ion milling. The sample conditions were referred to as as-built (AB), solution annealed (AN), and aging state (AG).

Figure 2(a) displays a region near a representative melt pool in the L-PBFed as-built specimen. The macroscopic fish-scaled melt pools have a depth of approximately 53 μm (Figure 2(b)). At the microscale inside the melt pools, PAGs can be observed, marked with white, red, and yellow colors. The as-built martensitic microstructure consists of small grains of PAGs, averaging around 8.75 μm, along with solidification cells confined by the PAGs. The cells exhibit a honeycomb structure elongated in the growth direction, with diameters typically ranging from 0.2 to 0.5 μm, depending on local solidification rates. Some of the cells are indicated by blue solid lines in Figure 2(a). These solidification cells represent colonies of PAG cells transformed to the martensitic structure during cooling. Figures 2(b) through (d) present the building direction inverse pole figure (BD-IPF) maps and grain size distribution plots of the martensitic structures and their corresponding reconstructed PAGs in the as-built and heat-treated states. Martensitic blocks were identified as bcc grains surrounded by high-angle grain boundaries (HAGBs) with a misorientation exceeding 15 deg. The IPF maps of reconstructed PAGs, alongside original martensitic structures, are displayed in the as-built and solution annealing states (Figures 2(b) and (c)). After solution annealing, noticeable growth occurred in block sizes (averaging roughly 3.83 μm in AB) and PAGs (averaging about 8.75 μm initially), expanding approximately 2.2 and 2.9 times, respectively. Following solution annealing, block sizes and PAG averages achieve around 8.33 and 25.40 μm, correspondingly. However, the block size, approximately 8.8 μm in the AG state, remains nearly unaltered post aging.

TEM images in Figure 2 depict the laths of martensitic structures in three states. Average lath width increased after solution annealing and remained constant during aging. Larger martensitic blocks were formed in the solution annealed state due to transformation within the parent austenite grains (PAGs). The L-PBF process with intense temperature differences induces Marangoni convection, leading to impurity accumulation and dislocation concentration at cell boundaries. This renders the solidification cells metastable and prone to recrystallization and growth of grains within heat treatment.[7,24] Consequently, the PAGs generated during solution annealing are larger than those originating from solidification in their initial form. As martensite transforms within PAGs, blocks double in size post-annealing *vs* initial as-built dimensions. The nearly constant grain structure observed during aging is influenced by particle pinning, assessed through modified analyses based on Zener and Smith's work.[25] Furthermore, TEM and HAADF-STEM analyses of the AG sample revealed the presence of nanoscale spherical oxide inclusions and other precipitates, mainly composed of Al, O, and N. These nanoscale incoherent precipitates exert a pinning effect on grain boundary movement, hindering further grain growth during the aging process.[25] The STEM data in Figure 2(d) include the Nb element. This addition was prompted by an estimated 0.09 wt pct of Nb in the gas-atomized CX powder, determined through X-ray fluorescence (XRF) measurements (refer to electronic supplementary Table S-I).

To gain a deeper understanding of the microstructural changes during the heat-treatment process, a specific melt pool was chosen from the IPF map of the as-built sample. This melt pool is highlighted by broken lines in Figures 2(b) through (d). Figures 3(a) through (f) present the cropped melt pool at higher magnification,

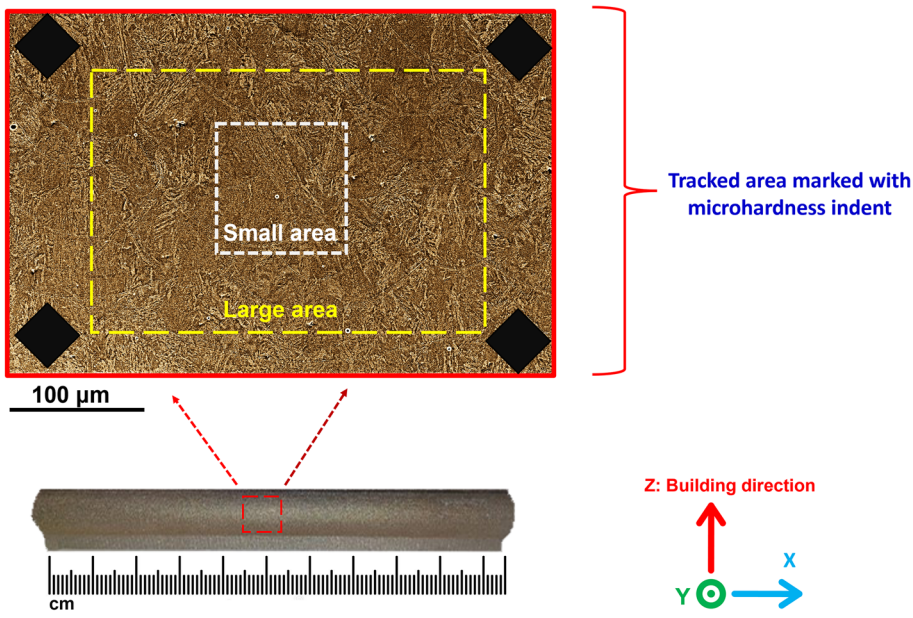

Nominal composition of the powder of CX stainless steel (wt.%)

Element	C	Ni	Cr	Mo	Al	Mn	Si	Fe
wt.%	<0.05	8.4-10	11-13	1.1-1.7	1.2-2	0.4	0.4	Bal.

Process parameters according to EOS GmbH recommendation

Laser power (W)	Scan speed (mm/s)	Hatch space (µm)	Layer thickness (µm)	Rotation of successive layers
258	1066.7	100	30	67°

Fig. 1—An image of the rod-shaped CX SS sample printed horizontally, and the *X-Z* plane cut from the sample marked with the microhardness indents for tracking microstructure. The small and large area for microstructural tracking using quasi in situ EBSD as well as the process parameters used for its fabrication are also shown.

along with BD-IPFs of martensitic structures and corresponding KAM maps in three states (AB, AN, and AG). Additionally, grain aspect ratio maps of reconstructed PAGs in AB and AN states, along with plots depicting the distribution of minor (d_{min}) to major (d_{max}) axis ratio of PAGs grains, are illustrated in Figures 3(g) through (i). In addition, two areas, named A and B areas, are distinguished in the cropped melt pool in the as-built, and heat-treated conditions (Figures 3(d) through (h)). Analysis of IPF maps (Figures 3(a) through (c)) reveals a transition from a finer microstructure in the as-built state to a larger, more equiaxed structure in the heat-treated states. Martensitic structures in AN and AG states exhibit similarity in size and morphology. Comparing PAGs grain aspect ratio maps in as-built and solution annealing (Figures 3(g) and (h)) confirms the evolution of more equiaxed PAGs grains in the AN state. Furthermore, distribution plots of the d_{min}/d_{max} ratio of PAGs in AB state from areas A and B (Figure 3(i)) depict a broader distribution and a higher proportion of high grain aspect ratios ($d_{min}/d_{max} \geq 0.5$) in PAGs of area B compared to those in area A. This observation suggests that the blocks within the PAGs in area B possess a more equiaxed morphology than those in area A.[26,27]

In addition, the KAM map of the cropped melt pool (Figures 3(d) through (f)) reveals a distinction between the martensitic structures in areas A and B in the as-built state. Interestingly, the high KAM value region, indicating higher dislocation density, corresponds to area B rather than area A in the as-built condition. Furthermore, the solution annealing and aging processes led to a uniform microstructure with low KAM values in most regions of the cropped area after annealing. Figures 3(a) through (c) also depict the calculated values of austenite volume fractions for the cropped melt pool in the as-built and heat-treated states. In the as-built state, a small fraction of retain/reverted austenite (RA) is estimated. However, after the solution annealing and aging processes, no evidence of austenite is detected (see Electronic Supplementary Figure S-1). The results align with our previous studies[28] on horizontal printed samples, showing consistency with the XRD results for the as-built and heat-treated conditions. The as-built sample exhibited a higher volume fraction of retain/reverted austenite (RA) at approximately 12 pct, while the solution annealed and aged sample showed almost no detectable austenite.[28]

The average grain size (d) of area A and B shown in the cropped melt pool (Figure 3) in three states is plotted

in Figure 4(a). In addition, Figure 4(b) exhibits the trend of the recrystallization and grain growth, which happened in both areas (A and B) during the solution annealing process for one hour holding at 900 °C. Broken and solid lines are employed to connect points in Figures 4(a) and (b), enhancing the visual continuity for a clearer representation of the trend in changes. Also, the IPF maps of the cropped meltpool with area A and B in step times of 0, 10, 20, 30, 40, and 60 minutes during solution annealing are also shown in Supplementary Figure S-2 (refer to Electronic Supplementary Data File).

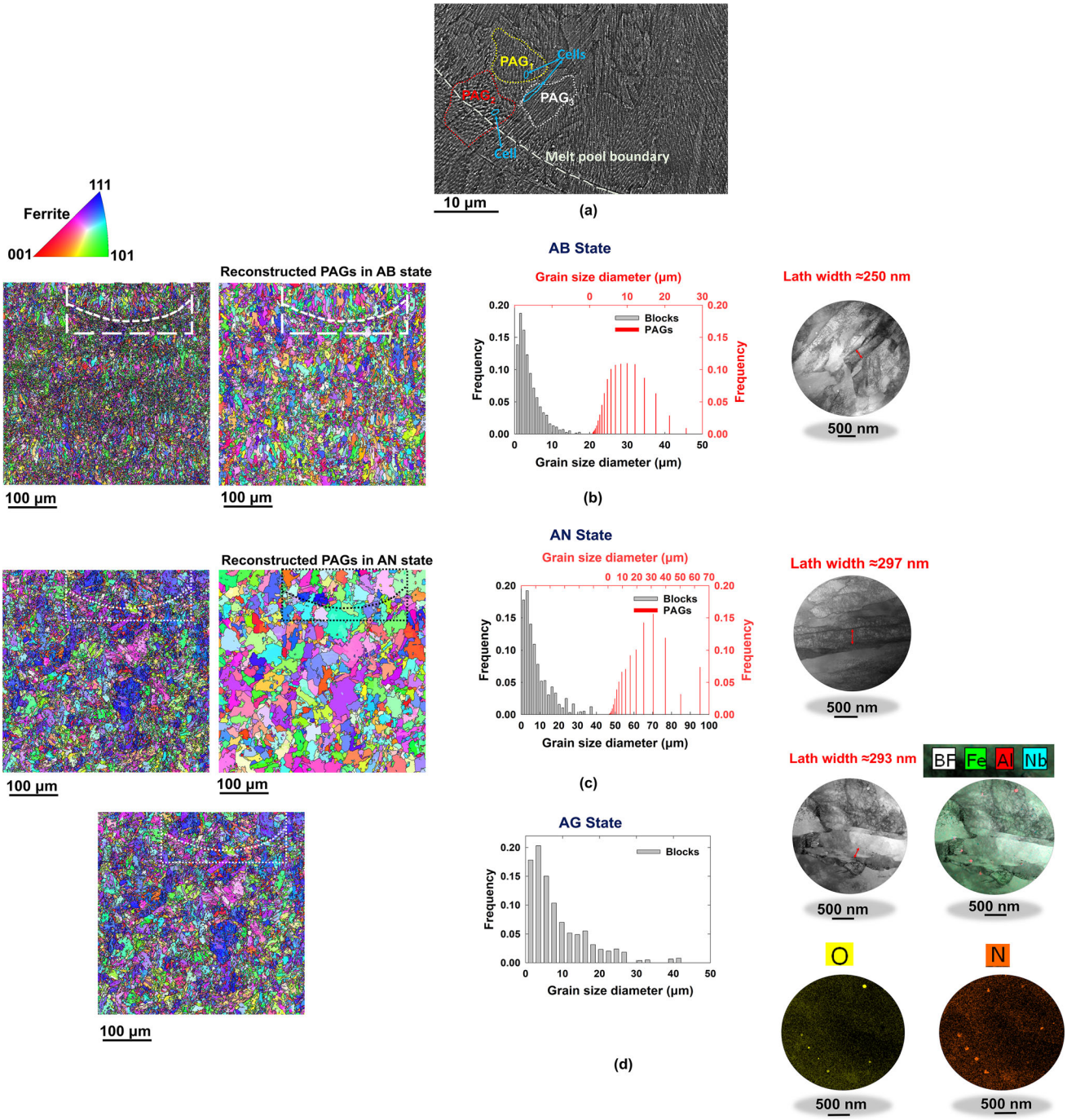

Fig. 2—(*a*) SEM image of a representative melt pool, broken white line indicates the melt pool boundary, and the yellow, red, and blue lines show some of PAGs including the cell shown in blue lines, (*b*) to (*d*) IPF color coding in building direction (BD) from the martensitic microstructure accompanied with the IPF of their reconstructed PAGs in the as-built (AB) and solution annealed (AN) states, the grain size distribution of martensite blocks and the corresponding PAGs are also shown as well in the TEM images taken from the laths. Also, the HAADF-STEM image and EDS maps from the TEM specimen related to the aging state are also shown in (d). A cropped melt pool is marked with broken white and black lines in (b) to (d) (Color figure online).

The grains distributed in area B grow to about three times after solution annealing, while the grains in area A are only 1.2 times larger than those observed in the as-built state. In addition, the average value of grain sizes in areas A and B in the solution annealed and aged states is converging to reach a more uniform grain structure after subsequent aging, whereby the value of d is almost the same for areas A and B. An increase in grain size was observed in the martensitic structure of area B immediately after heating up to 900 °C. The average grain size, which was around 2.5 μm in the as-built state, reaches approximately 3.6 μm at the moment of reaching 900 °C (time = 0). On the other hand, in area A, a reduction in grain size was noticeable. The grain size, which was approximately 5.3 μm in the as-built state, decreases to about 4.2 μm upon reaching the solution annealing temperature (time = 0).

The L-PBF process involves multiple rapid heating and cooling cycles, which can lead to the *in-situ* partitioning of austenite stabilizer elements within the inner layers. This phenomenon is more likely to occur in areas within the heat-affected zones (HAZ) or below the boundaries of the melt pool, where temperatures can approach the A_{c1} point.[29,30] Consequently, it is possible to observe a solid-state transformation of austenite reversion in these regions. It is suggested that the fine and more equiaxed martensitic structures formed in area B are more prone to austenite reversion compared to those formed in area A. In the event of austenite reversion occurring in the fine martensitic structure beneath the melt pool boundary, a higher density of dislocations is induced in this area compared to area A.[31–33] The high density of dislocations in the areas of reverted austenite in area B makes a potent driving force for recrystallization and grain growth during subsequent heating. As a result, partial recrystallization and grain growth may occur, particularly in zones that have already transformed to austenite before reaching the solution annealing temperature. This observation is consistent with the average grain size results in the as-built state and the annealed condition at time = 0 of area B. The grain size of area B increased after heating up to 900 °C, indicating grain growth. However, when comparing the average value of grain size of area A in the as-built state and the annealed state at time = 0, a diminished grain size is noted, indicating only recrystallization in area A during the heating process up to 900 °C.

It can be observed that the average grain sizes in both areas decreased when subjected to a soaking time of 20 minutes during solution annealing (Figure 4(b)). The decrease in grain size during annealing may be linked to the recrystallization of austenite grains created during martensite (α) reversion. Earlier studies indicated that the austenite start temperature (A_{c1}) for $\gamma \leftrightarrow \alpha$ transformation in L-PBF CX samples is approximately 650 to 750 °C.[28] However, after this initial decrease, grain growth becomes the dominant mechanism. Consequently, the values of the grain growth stage (d) observed in areas A and B were plotted against the soaking times at the solution annealing temperature (Figures 4(c) and (d)).

The Sellars model for grain growth was employed, and a linear fit using Eq. [1][34] was applied to the experimental values depicted in Figures 4(c) and (d) as follows:

$$d^n = A \exp\left(\frac{-Q}{kT}\right) t, \qquad [1]$$

where d denotes average grain size (μm); t is holding time (min); T denotes heating temperature (K); K is Boltzmann constant (1.38×10^{-23} J/K); Q stands for activation energy for grain growth (J); and A and n are constants.[34–36] The fitting results reveal a consistent n value of 1.3 for both regions. In addition, the value of Q for the grain growth in areas A and B is estimated as follows:

$$Q_{\text{areaA}} = 8.8 \times 10^{-23}(\text{Ln A} + 1.8) \qquad [2]$$

$$Q_{\text{areaB}} = 8.8 \times 10^{-23}(\text{Ln A} + 1.9) \qquad [3]$$

The activation energy values shown in Eqs. [2] and [3] for areas A and B, respectively, are almost the same, indicating similar barrier energies for grain growth in martensitic structures. Thus, the key factors influencing growth extent are the driving force (determined by grain boundary density) and curvature resulting from dislocation accumulation.[37]

Figures 3(i) and 4(a) reveal that area B, below the melt pool boundary, displayed smaller equiaxed martensitic structures (average block size of 2.5 μm) and higher dislocation density compared to area A (Figure 3(d)). In contrast, area A consisted of larger columnar grains (average size of 5.3 μm). The formation of columnar martensitic structures in area A is attributed to the ratio of thermal gradient (G) to solidification rate (R), falling within the range of columnar-dendritic solidification. It is also known that the remelting of previous layers during the L-PBF process induces heterogeneous nucleation at the meltpool boundary and epitaxial grain growth with the columnar-dendritic structures in front.[38–40] The L-PBF process experiences high cooling rates ($G \times R$), leading to a refined microstructure. It is proposed that small equiaxed grains initially emerge on the upper surface of each melt pool, acting as nucleation sites for epitaxial grain growth of columnar structures in subsequent layers. Consequently, a finer and more equiaxed solidification structure is observed near the surface of the preceding melt pool, where the G/R ratio is lower compared to regions with columnar structures. In area B, below the cropped melt pool boundary, the fine equiaxed grains originated from the top surface of the previous fusion line in the underlying solid material, serving as seeds for the columnar structures observed in area A. Additionally, the austenite volume fraction calculations from the cropped melt pool (Figures 3(a) through (c) and S-1 in Electronic Supplementary Data File) and previous XRD results validate the existence of retained austenite in the as-built state. The accumulation of retained austenite is more pronounced in area B than in area A (Figures 3(a) and S-1 in the Electronic

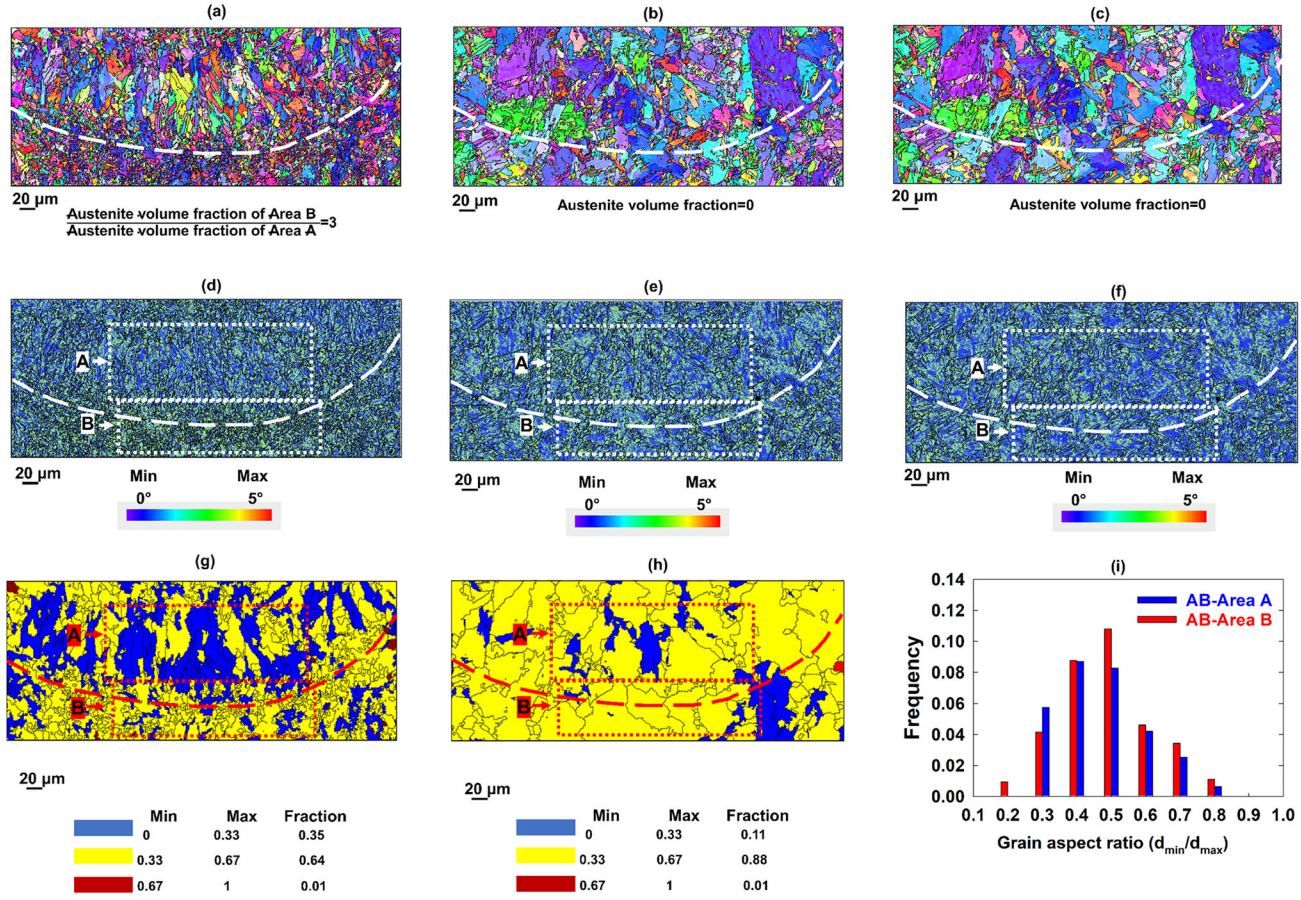

Fig. 3—EBSD measurements of the cropped melt pool in three states with two identified areas of A and B, (*a*) to (*c*): BD-IPF maps of the martensitic structures, (*d*) to (*f*) KAM maps of the original martensitic microstructure, (*g*) to (*h*) aspect ratio maps of reconstructed PAGs in AB and AN states, (*i*) chart of the grain aspect ratio of reconstructed PAGs in the as-built state of area A and B. In this figure, (a), (d), (g) are for the as-built state, (b), (e), (h) are related to the solution annealed condition, and (c) and (f) correspond to the subsequent aged state.

Supplementary File). This retained austenite presence hindered the growth of martensitic blocks in area B, leading to a finer block structure compared to area A.[41,42] The solidification parameters (G and R) and solid-state phenomena, including recrystallization and solid-state transformation, during the remelting and cooling stages of L-PBF, contribute to the development of a more equiaxed and finer martensitic structure with increased dislocation density below the melt pool boundary compared to the columnar structure within the melt pool area. The finer and more equiaxed martensitic structures exhibit higher curvature of the martensite/austenite interface, resulting in elevated elastic strain energy due to a denser interface dislocation and coherency strain (grain size effect). This indicates a stronger driving force for grain growth in area B than in area A.

In summary, in our quasi *in-situ* study of L-PBF fabricated martensitic stainless steel, significant findings emerged regarding microstructural changes during solution annealing and aging. Solidification features induced recrystallization and grain growth, doubling the grain size after solution annealing. However, Al–O–N–Nb particles acted as pinning agents, impeding further grain growth during aging. Analysis revealed partial recrystallization and growth in finer, equiaxed structures below the melt pool boundary, contrasting with larger, columnar structures within the melt pool. This suggests that solidification parameters and *in-situ* solid-state transformation in L-PBF create a stronger driving force for recrystallization and growth in finer grains, while limited growth occurs in larger columnar grains. These findings emphasize the complex interplay of solidification, recrystallization, and grain growth in L-PBF martensitic stainless steel, where solidification features and particle pinning determine the microstructure during heat treatment.

ACKNOWLEDGMENTS

The authors acknowledge funding from the Natural Sciences and Engineering Research Council of Canada (Grant RGPIN-2016-04221), Atlantic Canada Opportunities Agency, Atlantic Innovation Fund (Project

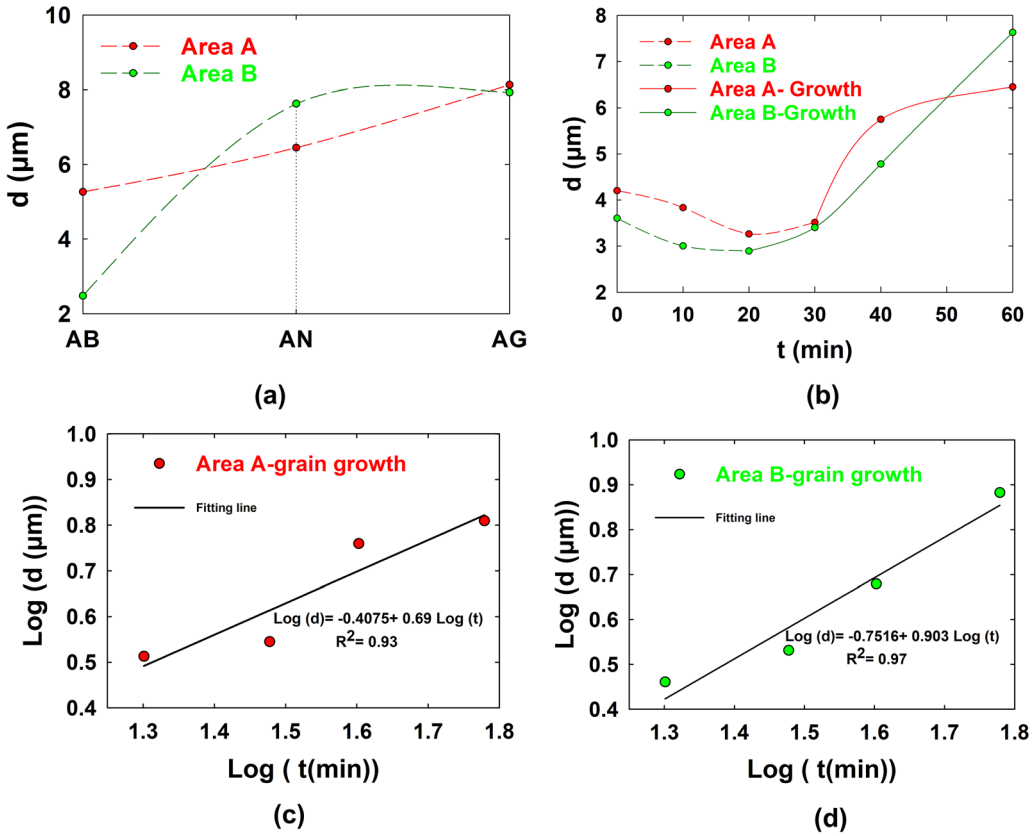

Fig. 4—Average grain size of the martensitic microstructure in area A and B from the cropped melt pool, (*a*) data of the changes in average grain size in three states (as-built, solution annealed, and aging), (*b*) average grain size *vs* time during the solution annealing at 900 °C for 1 hour for the area A and B form the cropped melt pool, (*c*) and (*d*) log–log plots of the grain growth stage during the solution annealing for area A and B with corresponding fitting lines.

210414), New Brunswick Innovation Foundation (Grant RIF2017-071), and Mitacs Accelerate Program (Grant IT10669)

CONFLICT OF INTEREST

The authors declare that they have no conflict of interest.

SUPPLEMENTARY INFORMATION

The online version contains supplementary material available at https://doi.org/10.1007/s11661-024-07353-4.

REFERENCES

1. R. Schnitzer, R. Radis, M. Nöhrer, M. Schober, R. Hochfellner, S. Zinner, E. Povoden-Karadeniz, E. Kozeschnik, and H. Leitner: *Mater. Chem. Phys.*, 2010, vol. 122, pp. 138–45.
2. V. Seetharaman, M. Sundararaman, and R. Krishnan: *Mater. Sci. Eng.*, 1981, vol. 47, pp. 1–11.
3. H. Asgari and M. Mohammadi: *Mater. Sci. Eng. A*, 2018, vol. 709, pp. 82–89.
4. M.W. Wu, S.W. Ku, H.W. Yen, M.H. Ku, S.H. Chang, K. Ni, Z.S. Shih, C. Tsai, T.W. Hsu, C.L. Li, and C.K. Wang: *Mater. Sci. Eng. A*, 2023, vol. 887, 145744.
5. A. Shahriari, J. Samei, M. Sanjari, M. Jahanbakht, B.S. Amirkhiz, and M. Mohammadi: *Npj Mater. Degrad.*, 2022, vol. 6, pp. 1–19.
6. D. Dong, C. Chang, H. Wang, X. Yan, W. Ma, M. Liu, S. Deng, J. Gardan, R. Bolot, and H. Liao: *J. Mater. Sci. Technol.*, 2021, vol. 73, pp. 151–64.
7. K.G. Prashanth and J. Eckert: *J. Alloys Compd.*, 2017, vol. 707, pp. 27–34.
8. F.S.H.B. Freeman, J. Sharp, J. Xi, and I. Todd: *Addit. Manuf.*, 2019, vol. 30, 100917.
9. D. Kong, C. Dong, S. Wei, X. Ni, L. Zhang, R. Li, L. Wang, C. Man, and X. Li: *Addit. Manuf.*, 2021, vol. 38, 101804.
10. Y.M. Wang, T. Voisin, J.T. McKeown, J. Ye, N.P. Calta, Z. Li, Z. Zeng, Y. Zhang, W. Chen, T.T. Roehling, R.T. Ott, M.K. Santala, P.J. Depond, M.J. Matthews, A.V. Hamza, and T. Zhu: *Nat. Mater.*, 2017, vol. 17, pp. 63–71.
11. S. Morito, A.H. Pham, T. Ohba, T. Hayashi, T. Furuhara, and G. Miyamoto: *Microscopy*, 2017, vol. 66, pp. 380–87.
12. S. Morito, Y. Adachi, and T. Ohba: *Mater. Trans.*, 2009, vol. 50, pp. 1919–23.
13. R.A. Abrahams: The Development of High Strength Corrosion Resistant, PhD dissertation, The Pennsylvania State University, 2010.
14. H. Ramadas, S. Sarkar, P. Ganesh, R. Kaul, J.D. Majumdar, and A.K. Nath: *Mater. Sci. Eng. A*, 2023, vol. 866, 144657.
15. C. Cayron, A. Baur, and R. Logé: *Mater. Des.*, 2018, vol. 154, pp. 81–95.
16. R.J. Hamlin and J.N. DuPont: *Metall. Mater. Trans. A*, 2017, vol. 48A, pp. 246–64.

17. H. Chae, M.Y. Luo, E.W. Huang, E. Shin, C. Do, S.K. Hong, W. Woo, and S.Y. Lee: *Mater. Charact.*, 2022, vol. 184, 111645.
18. S. An, D.R. Eo, I. Sohn, and K. Choi: *J. Mater. Sci. Technol.*, 2023, vol. 166, pp. 47–57.
19. X.D. Nong, X.L. Zhou, J.H. Li, Y.D. Wang, Y.F. Zhao, and M. Brochu: *Scr. Mater.*, 2020, vol. 178, pp. 7–12.
20. W. Chen, L. Xu, K. Hao, Y. Zhang, L. Zhao, Y. Han, Z. Liu, and H. Cai: *Opt. Laser Technol.*, 2023, vol. 157, 108711.
21. J. Zhang, M. Wang, L. Niu, J. Liu, J. Wang, Y. Liu, and Z. Shi: *J. Alloys Compd.*, 2021, vol. 877, 160062.
22. C. Chang, X. Yan, R. Bolot, J. Gardan, S. Gao, M. Liu, H. Liao, M. Chemkhi, and S. Deng: *J. Mater. Sci.*, 2020, vol. 55, pp. 8303–16.
23. E. Gomes de Araujo, H. Pirgazi, M. Sanjari, M. Mohammadi, and L.A.I. Kestens: *J. Appl. Crystallogr.*, 2021, vol. 54, pp. 569–79.
24. N. Chakraborty: *Appl. Therm. Eng.*, 2009, vol. 29, pp. 3618–31.
25. P.A. Manohar, M. Ferry, and T. Chandra: *ISIJ Int.*, 1998, vol. 38, pp. 913–24.
26. J. Hidalgo and M.J. Santofimia: *Metall. Mater. Trans. A*, 2016, vol. 47A, pp. 5288–5301.
27. H.J. Kim, Y.H. Kim, and J.W. Morris: *ISIJ Int.*, 1998, vol. 38, pp. 1277–85.
28. A. Shahriari, M. Sanjari, H. Pirgazi, F. Fazeli, B. Shalchi Amirkhiz, L.A.I. Kestens, and M. Mohammadi: *Metall. Mater. Trans. A*, 2022, vol. 53A, pp. 1771–92.
29. P. Krakhmalev, I. Yadroitsava, G. Fredriksson, and I. Yadroitsev: *Mater. Des.*, 2015, vol. 87, pp. 380–85.
30. A.K. Bhaduri and S. Venkadesan: *Steel Res.*, 1989, vol. 60, pp. 509–13.
31. G. Krauss: *Acta Metall.*, 1963, vol. 11, pp. 499–509.
32. C.A. Apple and G. Krauss: *Acta Metall.*, 1972, vol. 20, pp. 849–56.
33. N. Nakada, R. Fukagawa, T. Tsuchiyama, S. Takaki, and D. Ponge: *ISIJ Int.*, 2013, vol. 53, pp. 1286–88.
34. C.M. Sellars and J.A. Whiteman: *Met. Sci.*, 1979, vol. 13, pp. 187–94.
35. H.S. Yang and H.K.D.H. Bhadeshia: *Scr. Mater.*, 2009, vol. 60, pp. 493–95.
36. D. Xu, C. Ji, H. Zhao, D. Ju, and M. Zhu: *Sci. Rep.*, 2017, vol. 7, pp. 1–13.
37. C. Celada-Casero, J. Sietsma, and M.J. Santofimia: *Mater. Des.*, 2019, vol. 167, 107625.
38. S. Kou: *Welding Metallurgy*, 1st ed. Wiley, Hoboken, 2003, pp. 170–215.
39. T. Wang, Y.Y. Zhu, S.Q. Zhang, H.B. Tang, and H.M. Wang: *J. Alloys Compds*, 2015, vol. 632, pp. 505–13.
40. H.H. König, N.H. Pettersson, A. Durga, S. Van Petegem, D. Grolimund, A.C. Chuang, Q. Guo, L. Chen, C. Oikonomou, F. Zhang, and G. Lindwall: *Acta Mater.*, 2023, vol. 246, 118713.
41. Y. Sun, R.J. Hebert, and M. Aindow: *Mater. Des.*, 2018, vol. 156, pp. 429–40.
42. M. Mahmoudi, A. Elwany, A. Yadollahi, S.M. Thompson, L. Bian, and N. Shamsaei: *Rapid Prototyp. J.*, 2017, vol. 23, pp. 280–94.